Providing early warning for flooding in the Yellowstone National Park using ambient seismic noise

Bingxu Luo[1], Hejun Zhu[1,2,*] and David Lumley[1,2]

[1]Department of Sustainable Earth Systems Sciences, The University of Texas at Dallas

[2]Department of Physics, The University of Texas at Dallas

Key Points:

- The annual peaks of relative seismic velocity variations (dv/v) have an average 40 days lead-time to the water discharge in the YNP flooding area.
- The poroelastic dv/v simulation supports the effective precipitation as the major factor on the ambient seismic noise field.
- The dv/v variations integrate both hydrologic and temperature variables and tend to provide early warning for the YNP floods.

Corresponding author: Hejun Zhu, `hejun.zhu@utdallas.edu`

Abstract

We utilize twelve-year ambient seismic noise (ASN) recordings to measure near-surface seismic velocity variations (dv/v) within the YNP flooding watersheds. We have observed that the annual peaks of dv/v variations have two to three months lead-time in comparison to anomalous water discharges. Our analysis indicates that the annual cycle of dv/v is highly correlated with the effective precipitation, which takes into account the snowpack loading and melting water infiltration processes. The annual peaks of dv/v are likely caused by abnormal melt water, which exceed the water storage capacity of the land. Furthermore, the best-fit poroelastic model provides further evidence that precipitation factors primarily influence the variations of the seismic field. Our analysis successfully explains the indicative changes in dv/v prior to the 2014 and 2022 YNP floods. This study demonstrates the potential of using seismic observables to monitor and assess the risk of devastating floods in the YNP.

Plain Language Summary

We use a novel seismic technique to investigate the flood mechanism in the Yellowstone National Park and aim to provide early warning information for upcoming floods. The current flood monitoring system primarily relies on the widespread usage of water gauge stations, which offer real-time monitoring of surface water discharges but do not provide early flood indicators beforehand. Some space-based techniques have also been employed to monitor land water deficits and provide flood indexes. However, their applications may be limited due to their low spatial resolution and sparse monthly sampling. Our study demonstrates how seismic signals respond to near-surface hydrologic processes and explains the 2-3 month lead-time of our seismic measurements compared to anomalous water discharges in the summer. We anticipate further studies to develop this seismic technique as an efficient flood indicator that can be integrated with the current flood monitoring system.

Introduction

Flood events typically occur when there is an excessive amount of water that cannot be absorbed or processed by the land surface (J. T. Reager & Famiglietti, 2009; Girotto & Rodell, 2019). According to the Dartmouth Flood Observatory (`http://floodobservatory.colorado.edu/Archives`), there were a total of 5,131 flood events worldwide between 1985 and 2021. These events can be caused by heavy rainfall, snow/ice melt, tropical storms, dam breaks and other factors. Flood events are most likely to happen during the rainy season, when the land surface is already saturated and unable to store additional rainfall (J. T. Reager & Famiglietti, 2009). Moreover, the risk and frequency of severe flood events may increase due to global warming (Hirabayashi et al., 2013). Therefore, it is crucial to develop real-time flood monitoring and early warning systems to mitigate disasters and reduce damage costs. Currently, most flood monitoring systems rely on networks of gauging stations (Girotto & Rodell, 2019). For instance, the U.S. Geological Survey (USGS) operates the National Water Information System, which collects daily data on surface water, groundwater and water quality from over 13,500 stations across the country (`https://waterdata.usgs.gov/nwis`). However, this system falls short when it comes to forecast flood events days or months in advance, as it only provides real-time measurements of surface water discharge and lacks information on subsurface water storage capacity.

On the other hand, the Gravity Recovery and Climate Experiment (GRACE) mission consists of a pair of satellites that were firstly launched in March 2002. These satellites were later replaced with GRACE-FO in 2017 (`https://www2.csr.utexas.edu/grace`). This project aims to map spatial and temporal variations of the Earth's gravity fields, which have been utilized to characterize water storage capacity. These studies have suggested that it could be used as a precursor for detecting and estimating regional flood events several months in advance (Crowley et al., 2006; J. T. Reager & Famiglietti, 2009; Vishwakarma et al., 2013; Long et al., 2014; J. Reager et al., 2014; Zhou et al., 2017).

However, several limitations may prevent the usage of GRACE measurements as a flood forecasting tool, such as coarse spatial and temporal resolutions (around 1 arc degree and a monthly interval), and delayed product release (around 2 months behind real-time) (J. T. Reager et al., 2015; Girotto & Rodell, 2019).

Over the past few decades, seismologists have been attempting to retrieve empirical Green's functions between two seismographic stations by cross-correlating their continuous ambient seismic noise (ASN) recordings (Campillo & Paul, 2003; Shapiro & Campillo, 2004). In addition to mapping the spatial distribution of seismic velocities within the Earth's crust and uppermost mantle using dispersive Rayleigh and Love waves (Lin et al., 2008; Bensen et al., 2008), this ASN technique also enables us to estimate time-lapse changes of near-surface relative velocity (dv/v). These changes are primarily influenced by surface/body wave scattering and can be measured through coda wave interferometry (Poupinet et al., 1984; Snieder et al., 2002; Lecocq et al., 2014). This ASN-based dv/v technique has been successfully applied to monitor Earth's crustal responses to various events, such as volcanic eruptions (Sens-Schönfelder & Wegler, 2006), earthquake ruptures (Wegler & Sens-Schönfelder, 2007), ice sheet melting (Mordret et al., 2016; Toyokuni et al., 2018; Luo et al., 2023) and terrestrial water storage (Lecocq et al., 2017; Clements & Denolle, 2018; Mao et al., 2022; Zhang et al., 2023). The measured seasonal variation or long-term trend of dv/v can be used to further investigate changes in subsurface pore/effective pressure (Christensen & Wang, 1985; Tsai, 2011), liquid saturation (Bachrach & Nur, 1998; Nakata et al., 2022), porosity (Bachrach & Nur, 1998; Lumley, 2001) and microstructures (Grêt et al., 2006). Using this ASN interferometry for monitoring tectonic and environmental changes offers several advantages: (1) The dv/v signals can be measured with high temporal resolution due to the continuous recording of Earth's surface movements by seismic sensors; (2) Seismic stations can be deployed in situ and maintained at a relatively low cost compared to other space-borne sensors; (3) Fast processing procedures and almost real-time datasets allow us to calculate dv/v variations within a couple of hours after the events, making it highly efficient in responding to environmental hazards.

The 2022 historical flood occurred in the watersheds of three major streams in the Yellowstone National Park (YNP) inspires us to explore the application of the ASN interferometry in investigating flood events. Our objective is to analyze the variations of near-surface seismic velocity in response to hydrologic variables, and explore the potential usage of seismic observables to provide early warning information for flood events in the YNP.

Data and Methods

Measurements of relative seismic velocity variation (dv/v)

We obtain continuous seismic recordings from six broadband stations that are deployed alongside the Madison, Firehole and Gibbon rivers in northern YNP (Figure 1). The watersheds of these three rivers cover one of the most severely flooded areas on June 13, 2022. All seismic stations are belong to the Yellowstone National Park Seismograph Network, which is operated by the University of Utah (University of Utah, 1983). We collect continuous seismic recordings for a period of twelve years, from January 2012 to December 2023.

The MSNoise package (Lecocq et al., 2014) is utilized for performing ASN cross-correlation and dv/v measurements. First, we apply the preprocesses of demeaning, detrending, and filtering to all seismic traces within the frequency range of 0.05 to 3 Hz. The noise correlation functions (NCFs) are then calculated between the vertical components of each pair of stations. Next, we define the analysis duration as 86,400 s (one day) and divide the seismograms from these two stations into 1,800 s slices with a 50% overlap. To eliminate outliers (such as local seismic activity), we set the extreme limits as three times the root mean square of each slice. In addition, we conduct spectral whitening for each correlation slice (1,800 s). We save the daily NCFs and create a moving stack every 120 days, which serves as a robust approximation for empirical Green's functions. The reference NCF is obtained by stacking all the daily NCFs together. The final step involves measuring traveltime shifts (dt) between the daily and reference NCFs using a technique called moving-window cross spectrum (MWCS) (Clarke et al., 2011). The MWCS technique capitalizes on the similarity of Fourier phase spectra between the daily and reference NCFs, enabling the measurement of time shifts (dt) in unwrapped phases by solving a linear regression problem. Assuming that the relative seismic velocity change is homogeneous within the study area, we can express the relation as:

$$dv/v = -dt/t \quad , \tag{1}$$

where dt/t represents the daily averaged relative traveltime shift between the current and reference NCFs, which can be determined using a weighted linear regression. To obtain the regional homogeneous variation of dv/v, we calculate the median value of the measured dv/v from all fifteen station pairs, which involve six different stations. More information about the MWCS technique and the parameters we used can be found in supplementary Text S1 and Table S1. In addition, Figure S1 illustrates the MWCS workflow for the station pair YFT-YHL.

Robustness tests of dv/v measurements

We first test dv/v measurements by using other two horizontal components (Figure S2). Generally, the dv/v variations from all three components show similar trends. We also observe that all three components have recording gaps, which can lead to unusual high-frequency perturbations in the measurements. Therefore, for the following analysis, we choose the measured dv/v from the vertical components, which have fewer data gaps and more reliable measurements.

The depth sensitivity test suggests that changes in Rayleigh wave phase velocity are more sensitive to shallow depths with relatively higher frequency ranges (Figure S3). We then conduct dv/v tests with various frequency ranges to determine the primary frequency contributing to the hydrologic response (Figure S4). In comparison, the tested

dv/v with a frequency range from 0.7 to 0.9 Hz shows the most similar results to our current measurements from 0.1 to 0.8 Hz. This test is consistent with the depth sensitivity test, which indicates higher frequency ranges are more responsive to near-surface variations. However, we also note that all the narrow 0.2 Hz frequency ranges generate more short-term noise. To strike a balance between sensitivity to different depths and measurement quality, we choose the measured dv/v from a relatively wide frequency band of 0.1 to 0.8 Hz for the following analysis.

Furthermore, we perform dv/v tests using different measurement windows, ranging from direct to late coda arrivals. These measurement windows are determined by employing varying inter-distance velocities (3.0, 1.0 and 0.5 km/s, see in Figure S5). The results obtained from all measurement windows are consistent with each other (Figure S5), which suggest that the measured dv/v is robust across different phase arrivals. Moreover, we would like to highlight that the short measurement windows (40 s) include a greater amount of high-frequency perturbations, which may introduce bias to our observations. Therefore, our current selections, which involve a phase velocity of 2.0 km/s and a window length of 80 s provide us with the most robust dv/v measurements.

Results

The leading annual peaks of dv/v with respect to the YNP floods

One important feature of the measured regional dv/v variation is its strong annual cycle and long-term trend. Here, we attempt to fit the cycle mode of the measured dv/v using the following function:

$$F(t) = x_1 cos\left(\frac{2\pi(t - x_2)}{365d}\right) + x_3 cos\left(\frac{2\pi(t - x_4)}{182.5d}\right) \quad , \tag{2}$$

where the first cosine term in the equation is used to fit dv/v with a period of one year (365 days), while the second cosine term with a period of 6 months (182.5 days) is utilized to further adjust the shape of the function and improve its overall fit with the measurements. From the fitted cycle mode (shown in the two inset panels in Figure 2), we observe a gradual increase in velocity during winters and a rapid drop in velocity during the subsequent summers.

The second major feature of the measured dv/v is its comparison with the average water discharge data recorded by four USGS water gauging stations (Figure S6). In most years, the annual peaks of the dv/v in springs occur before the annual water discharge anomalies in the summers. In Figure 2, we highlight the annual peaks of both dv/v and water discharge anomalies with red and green bars, respectively. On average, the peaks of dv/v occur around 40 days earlier compared to the water discharge records. Specifically, we observe that the dv/v values dropped significantly (-0.11% and -0.15%) 92 and 62 days before the 2014 high discharge anomaly and the 2022 historical flood, respectively. These sharp drops correspond to the high discharge peaks in these two years. Furthermore, after removing the fitted annual cycles, we observe a long-term trend of the dv/v (red dashed curve in Figure 2), which is consistent with the long-term trend of discharge peaks. There were two additional reported flood events along the Madison River that are shown as high discharge anomalies in May of 2017 and 2018 (Figure 2). However, dv/v failed to precede these two events due to the incomplete records within two stations at that time (Figure S2). Therefore, our observations suggest that the measured dv/v tends to show a close relationship with local hydrologic variability. Next, we will investigate the major YNP flood inducer and explore its contribution to the seismic field.

Corresponding seasonal fluctuations between dv/v and precipitation

Flood monitoring often relies on the land surface's ability to absorb and process water. This variability is influenced by hydrologic factors such as water in plants, groundwater, soil moisture and snow (J. T. Reager & Famiglietti, 2009). A previous study on the catastrophic 2011 Missouri River flood was conducted based on a Catchment Land Surface model with GRACE-based data assimilation (J. T. Reager et al., 2015). This study found that snow water equivalent was the major variable that reached a record high level before this flood. Snow melting water contributes around 15% of the pre-flood, basin-wide water storage variability and serves as a significant indicator of high streamflow during the 2011 Missouri River flood (J. Reager et al., 2014). Therefore, to investigate the connection between dv/v and floods, we start from confirming the correlation between water discharge, snow melting and dv/v in the YNP case. To achieve this, we collected the mean snowmelt rate in May and June, which are two months with the most intense snow melting (Figure S7). The datasets used are from the ERA5 program, which provides the fifth generation of the European Centre for Medium-Range Weather Forecasts (ECMWF) reanalysis datasets (Hersbach et al., 2018). Figure 3A shows a highly consistent variability between these three factors, with relatively high levels in four flooding years (2014, 2017, 2018 and 2022) and relatively low levels in 2015, 2016 and 2021. This correlation suggests a close relationship between the YNP floods and snowmelt water equivalent, which may account for the significant drop in dv/v. To fully study the annual cycle of dv/v and determine the contributions from different precipitation variables, we then collected daily records of snowfall, snowmelt, rainfall and evaporation over the twelve-year period. All these datasets were provided by the ERA5 program (Hersbach et al., 2018) and then averaged over the station-covered area. Figure 3B shows that snowfall has the longest duration approximately covering from October to the following April. On the other hand, the snowmelt, which represents a large amount of water melted from accumulated snowpack on the surface, has a shorter duration but a higher rate and amount with peak levels in the spring. Rainfall is distributed between the two snow seasons and has a similar but weaker effect compared to snowmelt. Evaporation follows a typical annual cycle with a peak level in the summer, consistent with temperature variations.

Previous studies have indicated that hydrologic processes can affect near-surface velocity variations mainly through surface load/unload (Tsai, 2011; Mordret et al., 2016; Luo et al., 2023) and subsurface water saturation (Biot, 1956; Bachrach & Nur, 1998; Lumley, 2001; Nakata et al., 2022). These two processes typically result in changes in confining pressure or pore pressure, which in turn influence the effective pressure (p_{eff}) on the seismic field. Therefore, we consider surface snow accumulation and subsurface liquid water saturation as the two major hydrologic contributors. We introduce a new variable, namely the effective precipitation (P_e), to explain the variations in dv/v:

$$P_e = S_f - (S_m + R - E) \quad , \tag{3}$$

where S_f, S_m, R and E represent snowfall, snowmelt, rainfall and evaporation, respectively. P_e reflects the combined effects of precipitation on the seismic field (dv/v). Continuous positive P_e values (highly overlapped with snowfall in Figure 3B) are associated with surface snow loading before the melting seasons, resulting in a steady increase in dv/v. On the other hand, extreme negative P_e values indicate a large amount of water (mainly from snow melting) that needs to be processed by the land surface. This can lead to increased water saturation of pore spaces and a significant reduction in the water capacity of the land, correlating with a sharp drop in dv/v. In conclusion, we propose that the P_e variable allows us to establish a connection between floods and dv/v for the case of the YNP.

Recognizing that P_e is proportional to variations in dv/v, we apply a cross-wavelet transform method to measure their local similarity (Torrence & Compo, 1998) (see more details in supplementary Text S2). We observe lags between these two signals at different local steps, as indicated by the arrows in Figure 3C. On average, dv/v variations have a time lag of 81±25 days with respect to P_e. In Figure 3D, it is easier to observe the consistency between these two time series if we shift dv/v ahead by the measured 81 days. We will demonstrate this time lag of the seismic field in the "Discussion" section. Here, we highlight that although the dv/v variations occur after the variations in P_e, their annual peaks still precede water discharge anomalies, as well as flood occurrences in summers (Figure 2B).

Discussion

Possible mechanisms of the annual cycle of dv/v to hydrologic processes

We attempt to integrate a mutual precipitation-based mechanism that may explain the annual cycle of measured dv/v. Based on the response of poroelastic medium to hydrology-induced pressure variability (Bachrach & Nur, 1998; Tsai, 2011; Mordret et al., 2016), we establish a conceptual hydro-seismic model with two annual stages, as shown in Figure 4A. We also show the seismic depth sensitivity kernel that is averaged over the frequency range used in this study. In comparison with this model, we average annual precipitation variables and P_e, and apply the same processing to dv/v in Figure 4B.

In Figure 4A, the first stage is snowfall accumulation, which mainly occurs from October to the following April. According to poroelasticity, surface loading driven by snowstatic pressure can cause subsurface pore spaces to close and increase grain contact, resulting in an increase in effective pressure (p_{eff}) and near-surface seismic wave speeds (dv/v). The first stage is represented by the consistency between the positive P_e and the increase in dv/v (blue shades in Figure 4B). The second stage is melting and rainfall water infiltration/saturation (Figure 4A), which begins around April and lasts throughout the summer. At the end of the first stage, surface unloading causes subsurface pores to reopen. In addition, a large amount of water, led by melting water, begins infiltrating into the subsurface, significantly increasing the water saturation of the reopened pore spaces. Water-saturated porous media typically lead to an increase in pore pressure and a reduction in effective pressure p_{eff}, which in turn is controlled by shear modulus and density, resulting in a reduction in seismic wave velocity in the media (Lumley, 1996; Bachrach & Nur, 1998). The response of seismic wave speeds against a fluid-saturated porous medium has been well studied using the Biot-Gassmann theory (Gassmann, 1951; Biot, 1956, 1962), and more details can be found in supplementary Text S3. Therefore, the second stage is suggested by the consistency between the negative P_e and the decrease in dv/v (red shades in Figure 4B). After the second stage, water inputs largely cease, allowing time for the saturated water to diffuse. Correspondingly, dv/v tends to increase again, which will be caught up in the next annual cycle (Figure 4A). We suggest that these two annual stages do not work separately, as the snowfall and snowmelt seasons somewhat overlap. Here, we do not exclude other hydrologic factors, such as groundwater below the root zone, which may also contribute to dv/v variation and flood occurrence in the YNP case. Since the general water table level is included in our seismic sensitive range, and groundwater is suggested as the second potential contributor to the 2011 Missouri River flood (J. T. Reager et al., 2015). Unfortunately, its contribution cannot be evaluated due to the absence of continuous groundwater monitoring in the YNP flooding area. Therefore, our integrated model provides a reliable physical mechanism that the annual leading peaks of dv/v are primarily determined by the anomalous balanced precipitation (P_e) infiltration, which always occurs before water discharge in the summer.

Simulation of dv/v based on poroelasticity and thermoelasticity

To further support our integrated hydro-seismic model, we attempt to simulate the dv/v variation by invoking a mathematical framework and adapted parameters. Tsai (2011) provided an analytical solution for the near-surface strain field and seismic wave speed changes due to poroelastic stresses. We combine this framework and precipitation variables to model the periodic change of dv/v, which can be represented as:

$$dv/v(t) \propto p_{eff}(t - \Delta t) \approx \rho \cdot g \cdot P_e(t - \Delta t) \quad , \tag{4}$$

where ρ and g denote water density and gravitational acceleration, respectively. Δt represents the measured time lag of $dv/v(t)$ with respect to the precipitation variables. Here, we propose that the seismic wave speeds are proportional to the near-surface strain changes, which are driven by the effective pressure $p_{eff}(t)$. We approximate $p_{eff}(t)$ based on the previous balanced effective precipitation $P_e(t)$ (Figure 3B). More details about the derivation of $dv/v(t)$ from poroelasticity can be found in supplementary Text S4. We utilize the maximum peak-to-peak value of $P_e(t)$ to simulate the high-end amplitude of the applied effective pressure (Figure S8a). The simulated dv/v from the best-fitted poroelastic model is presented in Figures 2 and S8c, where we observe consistent amplitudes and phases with respect to the measured $dv/v(t)$. All parameters and their references can be found in Table S2. Although some parameters may have large uncertainties, such as the second Murnaghan constant and the thickness of the incompetent layer (Figure S9), this end-member model still provides a physical constraint for our analysis with all parameters falling within reasonable ranges.

As mentioned earlier, the $dv/v(t)$ shows an average lag of 81 days (Δt) in relation to the precipitation variables (Figure 3C). A similar delay in water infiltration (1-2 months) has also been observed in the 2011 Missouri River flood case (J. T. Reager et al., 2015). In this poroelastic model, the Δt is a result of subsurface pressure diffusion and is primarily influenced by the thickness and diffusivity of an incompetent sedimentary layer (Tsai, 2011; Mordret et al., 2016) (refer to supplementary Text S4 for a more detailed description of this time lag). In the YNP study region, there are extensive Quaternary unconsolidated deposits that cover our major watersheds (Lowry et al., 1993; Nolan & Miller, 1995). These deposits likely play a significant role in the delay of $dv/v(t)$ in response to pressure changes. We estimated the thickness of this incompetent layer to be 3.39 m using a grid search (Figure S9).

On the other hand, thermoelasticity is another important factor that often causes strains in elastic media and leads to changes in seismic speeds due to the medium's thermal expansion (Berger, 1975; Tsai, 2011). To assess the impact of the thermoelastic effects on the seismic field and compare it to hydrology-induced poroelasticity, we simulate another periodic dv/v variation based on the same framework but substituting the temperature driving force (Figure S8b) and the thermal expansion term (Tsai, 2011) (more details can be found in supplementary Text S4). When comparing the simulated dv/v from these two models, we observe that the amplitude of hydrology-based poroelastic

dv/v is greater than that of thermoelasticity (Figures 2 and S8c). Furthermore, we calculate that these two models have different time lags (Δt equals to 77 and 107 days for poroelasticity and thermoelasticity, respectively), which may result in different annual cycle modes for dv/v. To further investigate the effects of temperature on the seismic field and its contribution to the YNP floods, we performed another measurement of dv/v using four stations located in a non-flooding area in the YNP. These stations are represented by three gray triangles and station YFT in Figure 1. We have observed that the cycle mode obtained from data fitting is significantly different from the one observed in the flooding area (Figure S10). Based on our findings, we suggest that in the flooding areas, the balanced hydrologic factor P_e plays a major role in determining the cycle mode of dv/v. While, in non-flooding areas, the contribution of thermoelasticity on the seismic field may be more prominent, resulting in different annual cycle modes for dv/v.

Moreover, previous studies have also indicated that dv/v is capable of reflecting long-term trends in surface loading and temperature variations (Lecocq et al., 2017; Luo et al., 2023). In addition to the annual cycle, the measured dv/v in the flooding area also shows continuous increasing trends prior to high water discharge anomalies in 2014, 2017 and 2022. This is particularly evident in the significant change of $+3.0 \times 10^{-2}\%$ from 2021 to 2022 (red dashed curves in Figures 2 and S11). To better understand these trends, we compare the long-term trend of dv/v with the accumulated snowpack depth and surface temperature over the flooding area (Figure S11). It is reasonable to assume that the snowpack depth changes proportionally with surface temperature and contributes to the long-term trend of dv/v before 2017. However, from 2019 to 2022, the overall decreasing snowpack depth fails to explain the increasing trend in dv/v (Figure S11). During the periods without snowpack covering, we observed that the summer temperature after 2019 has a more consistent trend with dv/v, including an anomalous high temperature in the summer of 2021. Based on these observations, we suggest that successive anomalous high temperatures may further increase the grain size and reduce the pore spaces in the surface (Berger, 1975; Tsai, 2011). This, in turn, may reduce the water capacity of the surface land during the melting/rainfall season. Therefore, both snowpack loading and high temperature can mutually contribute to the increase in long-term trend of dv/v, potentially enhancing the risk of flooding.

Conclusion

Throughout our analysis of the twelve-year ASN records in the YNP flooding area, we suggest that the annual cycle of the measured seismic velocity variation (dv/v) is likely a response to local hydrologic variations. The annual peaks of the dv/v are possibly determined by the infiltration of effective precipitation (P_e), their leading occurrence potentially provides early warning information for water discharge anomalies in summers. The increasing long-term trend of dv/v may also indicate high surface snowpack capacity and temperature, likely enhancing the risk of upcoming floods. The poroelastic dv/v simulation supports our analysis that the effective precipitation may serve as the major driving force on the seismic field. Thus, we propose that further studies is necessary to develop this ASN technique as a quantitative flood predictor, and its applications for other flood scenarios (e.g., real-time rainfall, seawater inputs, riverbank break) may need to be evaluated. However, our study still offers a novel and insightful seismic sensing of the YNP flood case by integrating complex hydrologic processes. We anticipate that this ASN technique can be widely applied by taking advantage of dense seismic networks in other plains and basins.

Data Availability Statement

Continuous seismic records are from the Yellowstone National Park Seismograph Network, operated by University of Utah (University of Utah, 1983), which can be downloaded using the Obspy package (Beyreuther et al., 2010). Seismic interferometry and dv/v measurements are performed using the MSNoise package (Lecocq et al., 2014). Water discharge time series are collected from the U.S. Geological Survey, National Water

Information System (`https://maps.waterdata.usgs.gov/mapper`). The datasets for different precipitation variables, surface temperature and snowmelt rate are collected from the ERA5 program (Hersbach et al., 2018). The root zone soil moisture datasets are collected from NASA's GRACE-FO measurements (`https://nasagrace.unl.edu`). All figures are plotted using the Matplotlib package (Hunter, 2007).

Acknowledgments

This research is supported by U.S. National Science Foundation Grant Number EAR2042098.

References

Bachrach, R., & Nur, A. (1998). High-resolution shallow-seismic experiments in sand, part i: Water table, fluid flow, and saturation. *Geophysics*, *63*(4), 1225-1233. doi: 10.1190/1.1444423

Bensen, G. D., Ritzwoller, M. H., & Shapiro, N. M. (2008). Broadband ambient noise surface wave tomography across the united states. *Journal of Geophysical Research: Solid Earth*, *113*(B5). doi: https://doi.org/10.1029/2007JB005248

Berger, J. (1975). A note on thermoelastic strains and tilts. *Journal of Geophysical Research (1896-1977)*, *80*(2), 274-277. Retrieved from `https://agupubs.onlinelibrary.wiley.com/doi/abs/10.1029/JB080i002p00274` doi: https://doi.org/10.1029/JB080i002p00274

Beyreuther, M., Barsch, R., Krischer, L., Megies, T., Behr, Y., & Wassermann, J. (2010, 05). ObsPy: A Python Toolbox for Seismology. *Seismological Research Letters*, *81*(3), 530-533. doi: 10.1785/gssrl.81.3.530

Biot, M. A. (1956). Theory of Propagation of Elastic Waves in a Fluid-Saturated Porous Solid. I. Low-Frequency Range. *The Journal of the Acoustical Society of America*, *28*(2), 168-178. doi: 10.1121/1.1908239

Biot, M. A. (1962). Mechanics of deformation and acoustic propagation in porous media. *Journal of Applied Physics*, *33*(4), 1482-1498. doi: 10.1063/1.1728759

Biot, M. A., & Willis, D. G. (1957, 06). The Elastic Coefficients of the Theory of Consolidation. *Journal of Applied Mechanics*, *24*(4), 594-601. Retrieved from `https://doi.org/10.1115/1.4011606` doi: 10.1115/1.4011606

Campillo, M., & Paul, A. (2003). Long-range correlations in the diffuse seismic coda. *Science*, *299*(5606), 547-549. doi: 10.1126/science.1078551

Christensen, N. I., & Wang, H. F. (1985). The influence of pore pressure and confining pressure on dynamic elastic properties of berea sandstone. *Geophysics*, *50*(2), 207-213. doi: 10.1190/1.1441910

Clarke, D., Zaccarelli, L., Shapiro, N. M., & Brenguier, F. (2011, 08). Assessment of resolution and accuracy of the Moving Window Cross Spectral technique for monitoring crustal temporal variations using ambient seismic noise. *Geophysical Journal International*, *186*(2), 867-882. doi: 10.1111/j.1365-246X.2011.05074.x

Clements, T., & Denolle, M. A. (2018). Tracking groundwater levels using the ambient seismic field. *Geophysical Research Letters*, *45*(13), 6459-6465. doi: https://doi.org/10.1029/2018GL077706

Crowley, J. W., Mitrovica, J. X., Bailey, R. C., Tamisiea, M. E., & Davis, J. L. (2006). Land water storage within the congo basin inferred from grace satellite gravity data. *Geophysical Research Letters*, *33*(19). doi: https://doi.org/10.1029/2006GL027070

Gassmann, F. (1951). Uber die elastizitat poroser medien. *Veirteljahrsschrift der Naturforschenden Gesellschaft in Zzirich*, *96*, 1-23.

Girotto, M., & Rodell, M. (2019). Terrestrial water storage. In (p. 41-64). doi: 10.1016/B978-0-12-814899-0.00002-X

Grêt, A., Snieder, R., & Scales, J. (2006). Time-lapse monitoring of rock properties with coda wave interferometry. *Journal of Geophysical Research: Solid Earth*, *111*(B3). doi: https://doi.org/10.1029/2004JB003354

Hersbach, H., Bell, B., Berrisford, P., Biavati, G., Horányi, A., Muñoz Sabater, J., ... Thépaut, J.-N. (2018). Era5 hourly data on single levels from 1959 to present. *Copernicus Climate Change Service (C3S) Climate Data Store (CDS)*. doi: 10.24381/cds.adbb2d47

Hirabayashi, Y., Roobavannan, M., Koirala, S., Konoshima, L., Yamazaki, D., Watanabe, S., ... Kanae, S. (2013). Global flood risk under climate change. *Nature Climate Change*, *3*, 816-821. doi: 10.1038/nclimate1911

Hunter, J. D. (2007). Matplotlib: A 2d graphics environment. *Computing in Science & Engineering*, *9*(3), 90–95. doi: 10.1109/MCSE.2007.55

Iverson, N. R., Baker, R. W., & Hooyer, T. S. (1997). A ring-shear device for the study of till deformation: Tests on tills with contrasting clay contents. *Quaternary Science Reviews*, *16*(9), 1057-1066. Retrieved from `https://www.sciencedirect.com/science/article/pii/S027737919700036X` doi: https://doi.org/10.1016/S0277-3791(97)00036-X

Lecocq, T., Caudron, C., & Brenguier, F. (2014). MSNoise, a python package for monitoring seismic velocity changes using ambient seismic noise. *Seismological Research Letters*, *85*(3), 715-726. doi: 10.1785/0220130073

Lecocq, T., Longuevergne, L., Pedersen, H., Brenguier, F., & Stammler, K. (2017, 10). Monitoring ground water storage at mesoscale using seismic noise: 30 years of continuous observation and thermo-elastic and hydrological modeling. *Scientific Reports*, *7*. doi: 10.1038/s41598-017-14468-9

Lin, F.-C., Moschetti, M. P., & Ritzwoller, M. H. (2008, 04). Surface wave tomography of the western United States from ambient seismic noise: Rayleigh and Love wave phase velocity maps. *Geophysical Journal International*, *173*(1), 281-298.

Long, D., Shen, Y., Sun, A., Hong, Y., Longuevergne, L., Yang, Y., ... Chen, L. (2014). Drought and flood monitoring for a large karst plateau in southwest china using extended grace data. *Remote Sensing of Environment*, *155*, 145-160. doi: https://doi.org/10.1016/j.rse.2014.08.006

Lowry, M. E., Smalley, M. L., Mora, K., Stockdale, R., & Martin, M. (1993). *Hydrology of park county, wyoming, exclusive of yellowstone national park* (Tech. Rep.). US Dept. of the Interior, US Geological Survey; Earth Science Information Center, Open-File Reports Section. doi: https://doi.org/10.3133/wri934183

Lumley, D. E. (1996). Seismic time-lapse monitoring of subsurface fluid flow. *ProQuest Dissertations and Theses*, 168. Retrieved from `http://libproxy.utdallas.edu/login?url=https://www.proquest.com/dissertations-theses/seismic-time-lapse-monitoring-subsurface-fluid/docview/304306639/se-2`

Lumley, D. E. (2001). Time-lapse seismic reservoir monitoring. *GEOPHYSICS*, *66*(1), 50-53. doi: 10.1190/1.1444921

Luo, B., Zhang, S., & Zhu, H. (2023). Monitoring seasonal fluctuation and long-term trends for the greenland ice sheet using seismic noise auto-correlations. *Geophysical Research Letters*, *50*(7), e2022GL102146. doi: https://doi.org/10.1029/2022GL102146

Mao, S., Lecointre, A., van der Hilst, R., & Campillo, M. (2022). Space-time monitoring of groundwater fluctuations with passive seismic interferometry. *Nature Communications*, *13*, 4643. doi: 10.1038/s41467-022-32194-3

Mordret, A., Mikesell, T. D., Harig, C., Lipovsky, B. P., & Prieto, G. A. (2016). Monitoring southwest Greenland's ice sheet melt with ambient seismic noise. *Science Advances*, *2*(5), e1501538. doi: 10.1126/sciadv.1501538

Nakata, R., Jang, U.-G., Lumley, D., Mouri, T., Nakatsukasa, M., Takanashi, M., & Kato, A. (2022). Seismic time-lapse monitoring of near-surface microbubble water injection by full waveform inversion. *Geophysical Research Letters*, *49*(24), e2022GL098734. doi: https://doi.org/10.1029/2022GL098734

Nolan, B. T., & Miller, K. A. (1995). *Water resources of teton county, wyoming, exclusive of yellowstone national park* (Vol. 95) (No. 4204). US Department of the Interior, US Geological Survey; Denver, Colo. doi: https://doi.org/10.3133/wri954204

Poupinet, G., Ellsworth, W. L., & Frechet, J. (1984). Monitoring velocity variations in the crust using earthquake doublets: An application to the calaveras fault, california. *Journal of Geophysical Research: Solid Earth*, *89*(B7), 5719-5731. doi: https://doi.org/10.1029/JB089iB07p05719

Reager, J., Thomas, B., & Famiglietti, J. (2014). River basin flood potential inferred using grace gravity observations at several months lead time. *Nature Geoscience*, *7*, 588-592. doi: 10.1038/NGEO2203

Reager, J. T., & Famiglietti, J. S. (2009). Global terrestrial water storage capacity and flood potential using grace. *Geophysical Research Letters*, *36*(23). doi: https://doi.org/10.1029/2009GL040826

Reager, J. T., Thomas, A. C., Sproles, E. A., Rodell, M., Beaudoing, H. K., Li, B., & Famiglietti, J. S. (2015). Assimilation of grace terrestrial water storage observations into a land surface model for the assessment of regional flood potential. *Remote Sensing*, *7*(11), 14663–14679. doi: 10.3390/rs71114663

Sens-Schönfelder, C., & Wegler, U. (2006). Passive image interferometry and seasonal variations of seismic velocities at Merapi Volcano, Indonesia. *Geophysical Research Letters*, *33*(21). doi: https://doi.org/10.1029/2006GL027797

Shapiro, N. M., & Campillo, M. (2004). Emergence of broadband rayleigh waves from correlations of the ambient seismic noise. *Geophysical Research Letters*, *31*(7). doi: https://doi.org/10.1029/2004GL019491

Snieder, R., Grêt, A., Douma, H., & Scales, J. (2002). Coda wave interferometry for estimating nonlinear behavior in seismic velocity. *Science*, *295*(5563), 2253-2255. doi: 10.1126/science.1070015

Torrence, C., & Compo, G. P. (1998). A practical guide to wavelet analysis. *Bulletin of the American Meteorological Society*, *79*(1), 61 - 78. doi: 10.1175/1520-0477(1998)079⟨0061:APGTWA⟩2.0.CO;2

Toyokuni, G., Takenaka, H., Takagi, R., Kanao, M., Tsuboi, S., Tono, Y., ... Zhao, D. (2018). Changes in greenland ice bed conditions inferred from seismology. *Physics of the Earth and Planetary Interiors*, *277*, 81-98. doi: https://doi.org/10.1016/j.pepi.2017.10.010

Tsai, V. C. (2011). A model for seasonal changes in gps positions and seismic wave speeds due to thermoelastic and hydrologic variations. *Journal of Geophysical Research: Solid Earth*, *116*(B4). doi: https://doi.org/10.1029/2010JB008156

University of Utah. (1983). *Yellowstone national park seismograph network.* International Federation of Digital Seismograph Networks. Retrieved from `https://www.fdsn.org/networks/detail/WY/` doi: 10.7914/SN/WY

Vishwakarma, B., Jain, K., Sneeuw, N., & Devaraju, B. (2013). Mumbai 2005, bihar 2008 flood reflected in mass changes seen by grace satellites. *Journal of the Indian Society of Remote Sensing*, *41*. doi: 10.1007/s12524-012-0256-x

Wegler, U., & Sens-Schönfelder, C. (2007). Fault zone monitoring with passive image interferometry. *Geophysical Journal International*, *168*(3), 1029-1033. doi: 10.1111/j.1365-246X.2006.03284.x

Zhang, S., Luo, B., Ben-Zion, Y., Lumley, D. E., & Zhu, H. (2023). Monitoring terrestrial water storage, drought and seasonal changes in central oklahoma with ambient seismic noise. *Geophysical Research Letters*, *50*(17), e2023GL103419. Retrieved from `https://agupubs.onlinelibrary.wiley.com/doi/abs/10.1029/2023GL103419` (e2023GL103419 2023GL103419) doi: https://doi.org/10.1029/2023GL103419

Zhou, H., Luo, Z., Tangdamrongsub, N., He, L., Xu, C., & Li, Q. (2017). Characterizing drought and flood events over the yangtze river basin using the hust-grace2016 solution and ancillary data. *Remote Sensing*, *9*, 1100. doi: 10.3390/rs9111100

542 ## Figures

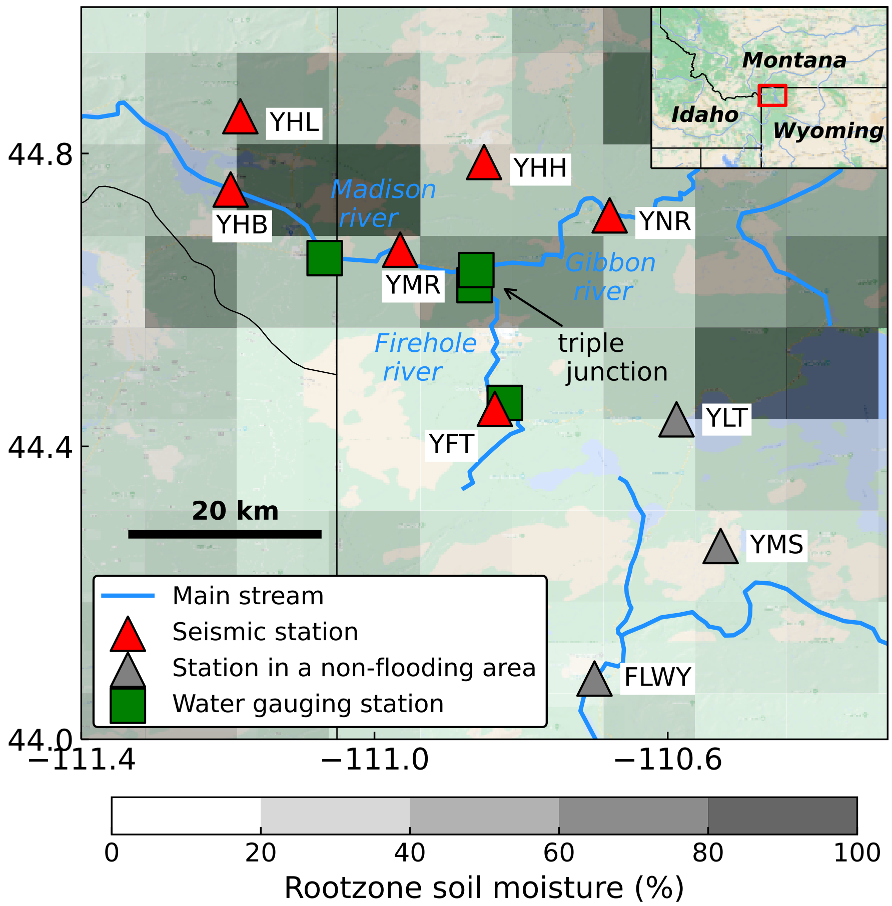

Figure 1: Seismo-hydrologic settings in the YNP. The cyan-blue curves represent major streams in the YNP. Red triangles and green squares denote six seismic and four USGS water stations, respectively. Gray triangles denote three seismic stations in a non-flooding area. The background grayscale represents the root zone (0-1 m depth) soil moisture measured in June 13, 2022 (https://nasagrace.unl.edu), which is reported as the peak level during the 2022 YNP flood. The junction of Madison, Firehole and Gibbon rivers covers one of the most severe flooding areas.

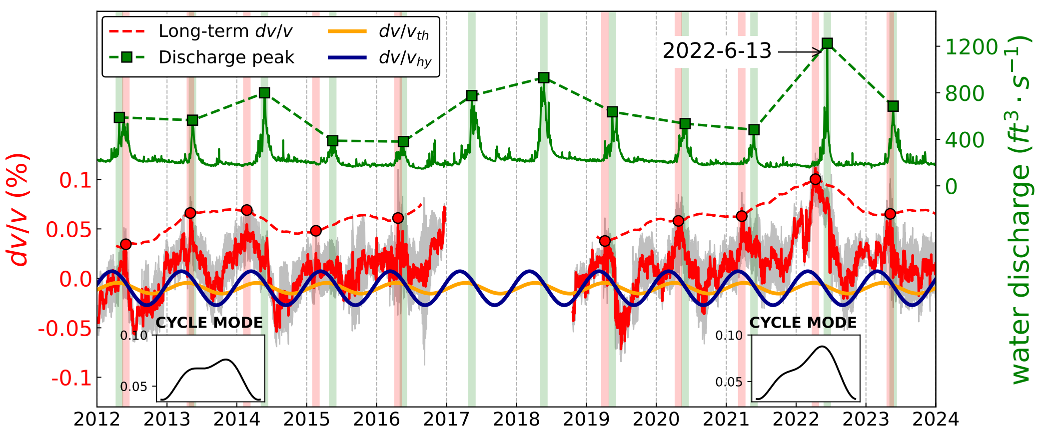

Figure 2: Seismic velocity variation (dv/v) in the flooding area. We compare the measured dv/v (in red) with the averaged water discharge (in green, https://maps.waterdata.usgs.gov/mapper). The annual peaks of dv/v and water discharge are marked by red solid dots and green squares, and are delineated in red and green bars, respectively. The cycle modes for two dv/v segments are fitted by using Equation 2. The long-term trend of dv/v is derived by removing the cycle mode and running 250 days moving average. Gray shades represent the misfits of dv/v measurements. Blue and orange curves are simulated dv/v based on hydrology-induced poroelasticity and thermoelasticity, respectively.

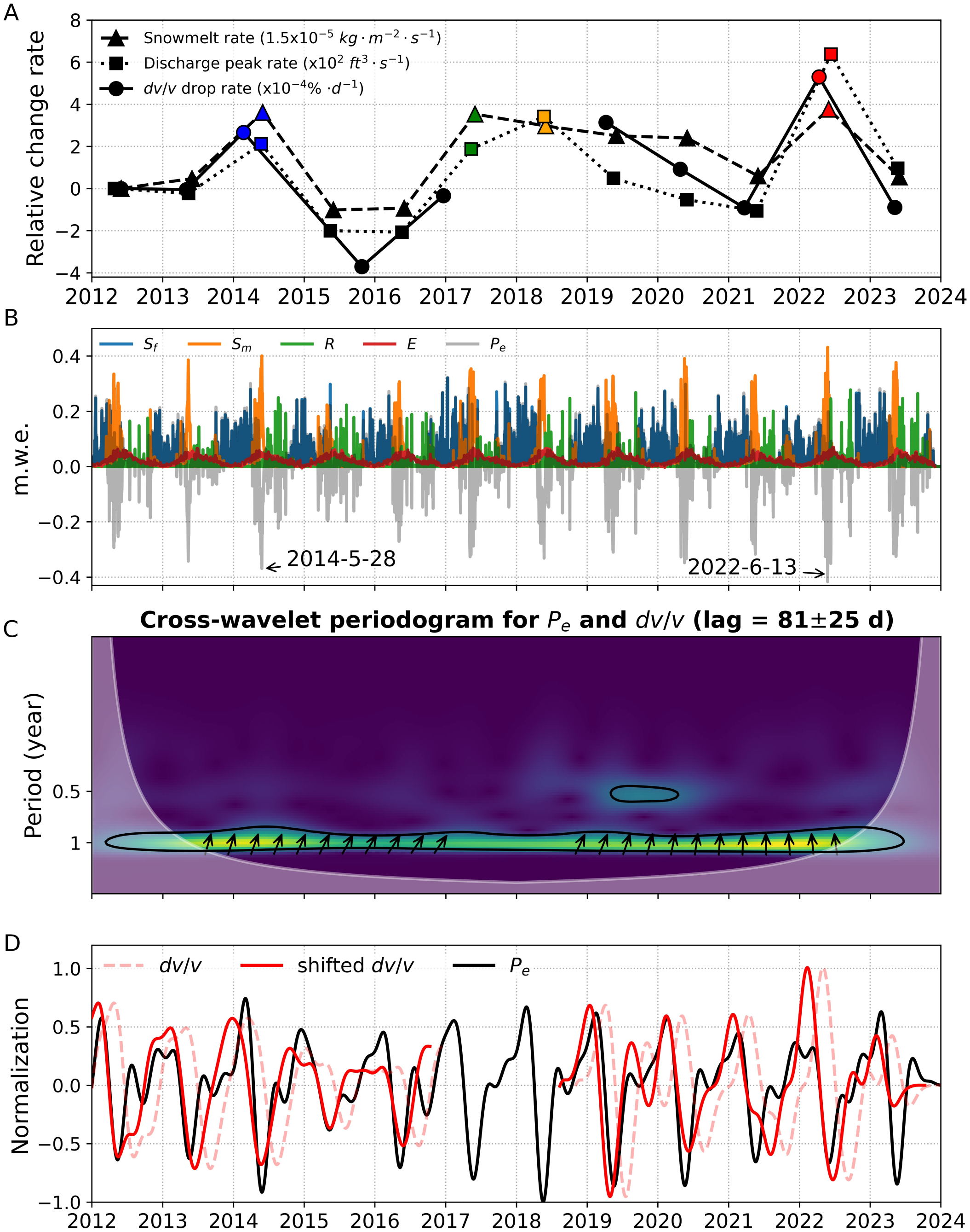

Figure 3: Correlation between seismic velocity variation (dv/v) with precipitation data. (A) Relative change rates of regional snowmelt, water discharge and dv/v. Four colors denote the YNP flooded years: 2014, 2017, 2018 and 2022. (B) The partition of different precipitation factors (S_f: snowfall; S_m: snowmelt; R: rainfall; E: evaporation) (Hersbach et al., 2018), and the effective precipitation (P_e) that is defined in Equation 3. The unit is water equivalent thickness in meters (m.w.e). (C) The cross-wavelet transform between P_e and dv/v. Arrows denote local phase shifts with the angle as time. The black contour represents a 99% confidence level against background noise. The averaged time lag of dv/v is 81 days (with a standard deviation of 25 days) with respect to P_e. (D) Correlation between P_e and shifted dv/v with 93 days. Both datasets are filtered in 8 to 36 months.

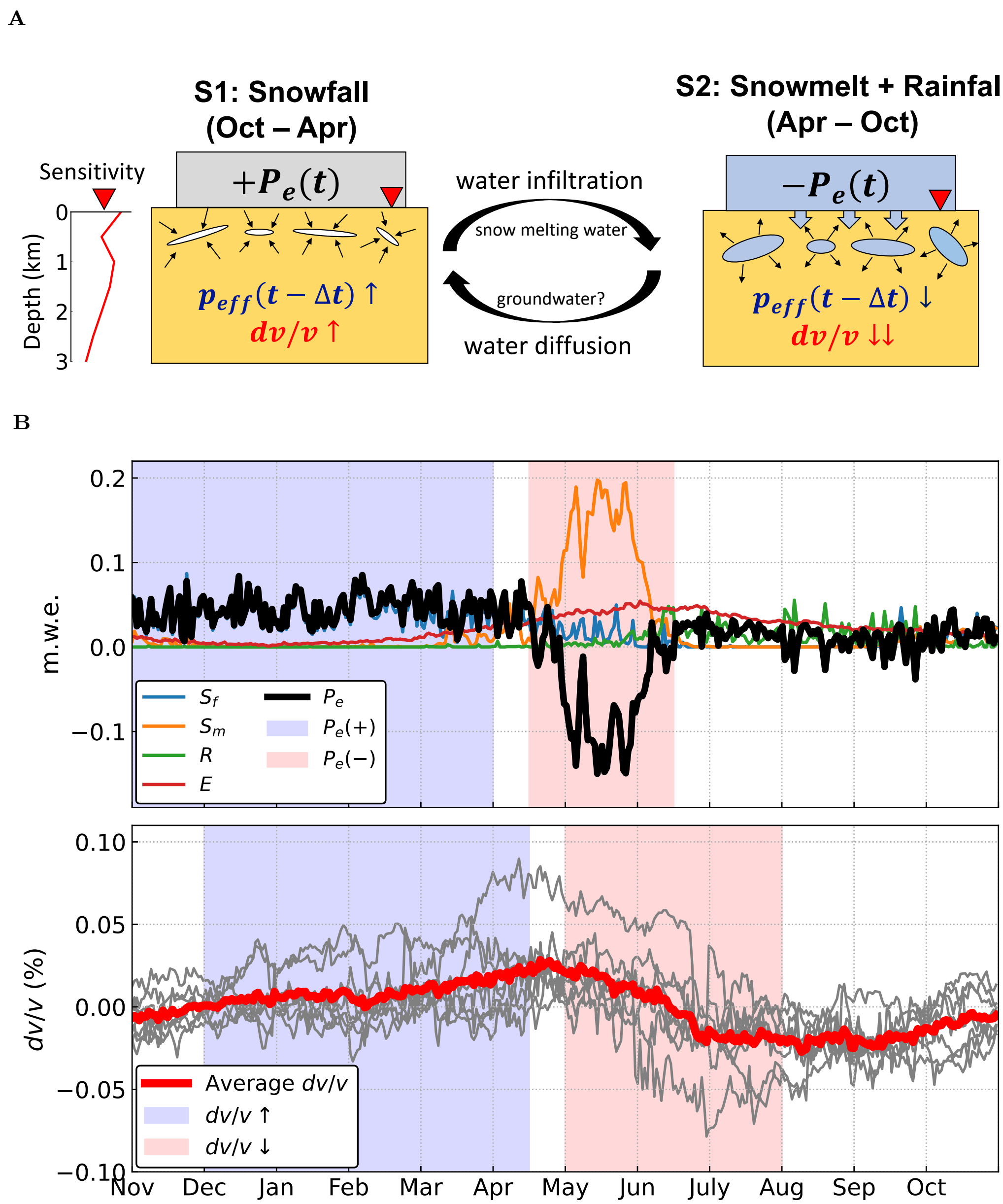

Figure 4: A physical mechanism for explaining the relation between dv/v and precipitation variables. (A) The conceptual hydro-seismic model includes two annual stages (S1 and S2). The red triangle denotes the seismic sensor. The averaged seismic depth sensitivity kernel is shown to the left side of S1. (B) Yearly averaged precipitation variables (top) and dv/v variation (bottom). Blue and red shades represent the positive and negative P_e, in turn drive the increase and decrease of dv/v, which are associated with Panel A.